nature physics

Supplementary information

https://doi.org/10.1038/s41567-024-02519-8

Continuity equation for the flow of Fisher information in wave scattering

In the format provided by the authors and unedited

Continuity Equation for the Flow of Fisher Information in Wave Scattering

S Supplementary Material

Here, we prove the central results of this paper in detail. In the first section, we show that the maximal FI for quasi-monochromatic waves of frequency ω measured by photodetectors in the far field can be described by a FI flux. By incorporating this flux into a continuity equation, we are able to identify FI sources, before we consider how absorption reduces the FI.

Next we consider in section S.3 how our algorithm on the FI sources can be used to explain the shape of the FI radiation patterns.

In section S.4 we make use of an adaptation of the FI operator to steer the flow of Fisher information in such a way that the information is effectively hidden from a potential eavesdropper.

Finally, in section S.5 and S.7 we highlight that the FI density can be viewed as the local information content of the wave by considering a weak detector in the near field and by showing that the total FI content in the photons is given by the integrated FI density in areas not in close proximity to the targets.

S.1 Fisher information of a photodetector in the far field

We start out by showing that the FI flux for quasi-monochromatic waves is an upper bound for the Fisher information that enters a detector in the far field. The detector measures the photon flux that hits the detector surface A with the mean photon flux [1]

$$\Phi_A(t) = (\hbar\omega)^{-1} \int_A \left\langle \boldsymbol{S}^{\mathrm{P}} \right\rangle_T (t) \cdot \mathrm{d}\boldsymbol{n}, \tag{1}$$

where $\boldsymbol{n}$ is the normal vector, which points in outgoing normal direction and the averaged Poynting vector

$$\left\langle \boldsymbol{S}^{\mathrm{P}} \right\rangle_T (t) = T^{-1} \int_{t-T/2}^{t+T/2} \boldsymbol{E}(\tilde{t}) \times \boldsymbol{H}(\tilde{t})\, \mathrm{d}\tilde{t}. \tag{2}$$

We assume that shot noise is the main source of noise; thus, the signal X is Poisson distributed with mean $T\Phi_A(t)$, i.e.

$$X(t) \sim P\left(T\Phi_A(t)\right), \tag{3}$$

for a photodetector measuring during the time interval $[t - T/2, t + T/2]$. For this noise model, the FI on a parameter θ at a single detector is given by

$$\mathcal{F}(\theta) = \frac{(T\partial_\theta \Phi_A)^2}{T\Phi_A}. \tag{4}$$

This can be rewritten to

$$\mathcal{F}(\theta) = \frac{(\int_{t-T/2}^{t+T/2} \int_A (\partial_\theta \boldsymbol{E} \times \boldsymbol{H} + \boldsymbol{E} \times \partial_\theta \boldsymbol{H}) \cdot \mathrm{d}\boldsymbol{n}\, \mathrm{d}\tilde{t})^2}{\hbar\omega \int_{t-T/2}^{t+T/2} \int_A (\boldsymbol{E} \times \boldsymbol{H}) \cdot \mathrm{d}\boldsymbol{n}\, \mathrm{d}\tilde{t}}. \tag{5}$$

If we place the detector outside the scattering region, we can assume that only outgoing plane waves impinge on the detector in outgoing normal direction $\boldsymbol{n}$. This gives us

$$\int_{t-T/2}^{t+T/2} \int_A (\boldsymbol{E} \times \boldsymbol{H}) \cdot \mathrm{d}\boldsymbol{n}\, \mathrm{d}\tilde{t} \geq 0 \tag{6}$$

for all $(\boldsymbol{E}, \boldsymbol{H})$.

Following a similar approach as in [2, Appendix A], we define a positive definite symmetric form $\langle \cdot, \cdot \rangle$ for two solutions $(\boldsymbol{E}_i, \boldsymbol{H}_i)$ for $i = 1, 2$ such that

$$\langle (\boldsymbol{E}_1, \boldsymbol{H}_1), (\boldsymbol{E}_2, \boldsymbol{H}_2) \rangle = \frac{1}{2\hbar\omega} \int_{t-T/2}^{t+T/2} \int_A (\boldsymbol{E}_1 \times \boldsymbol{H}_2 + \boldsymbol{E}_2 \times \boldsymbol{H}_1) \cdot \mathrm{d}\boldsymbol{n}\, \mathrm{d}\tilde{t}, \tag{7}$$

where the positive definiteness follows from eq. (6). Note that inserting the same state on both sides $\langle (\boldsymbol{E}, \boldsymbol{H}), (\boldsymbol{E}, \boldsymbol{H}) \rangle$ results in the average photon flow of $(\boldsymbol{E}, \boldsymbol{H})$ through the detector surface. For these forms, the Cauchy Schwartz inequality holds, which provides us with

$$\langle (\boldsymbol{E}_1, \boldsymbol{H}_1), (\boldsymbol{E}_1, \boldsymbol{H}_1) \rangle \langle (\boldsymbol{E}_2, \boldsymbol{H}_2), (\boldsymbol{E}_2, \boldsymbol{H}_2) \rangle \geq \left[\langle (\boldsymbol{E}_1, \boldsymbol{H}_1), (\boldsymbol{E}_2, \boldsymbol{H}_2) \rangle \right]^2. \tag{8}$$

Equality in relation (8) is satisfied for $\boldsymbol{E}_1 = \lambda \boldsymbol{E}_2$, $\boldsymbol{H}_1 = \lambda \boldsymbol{H}_2$ with a real scalar λ.

Finally, we note that in areas of free space, the derivatives of the fields, $\partial_\theta \boldsymbol{E}$ and $\partial_\theta \boldsymbol{H}$, also follow Maxwell's equations. Thus, by setting $(\boldsymbol{E}_1, \boldsymbol{H}_1) = (\boldsymbol{E}, \boldsymbol{H})$, $(\boldsymbol{E}_2, \boldsymbol{H}_2) = (\partial_\theta \boldsymbol{E}, \partial_\theta \boldsymbol{H})$ and inserting eq. (8) in the FI expression

(eq. (5)), we gain an upper bound for the FI,

$$\mathcal{F}(\theta) \leq 4(\hbar\omega)^{-1} \int_{t-T/2}^{t+T/2} \int_{A} (\partial_\theta \boldsymbol{E} \times \partial_\theta \boldsymbol{H}) \cdot \mathrm{d}\boldsymbol{n}\, \mathrm{d}\tilde{t}. \tag{9}$$

Due to the additivity of independent detectors with surfaces A_i, this can be extended to

$$\mathcal{F}(\theta) \leq 4(\hbar\omega)^{-1} \sum_i \int_{t-T/2}^{t+T/2} \int_{A_i} (\partial_\theta \boldsymbol{E} \times \partial_\theta \boldsymbol{H}) \cdot \mathrm{d}\boldsymbol{n}\, \mathrm{d}\tilde{t}. \tag{10}$$

For multiple detectors, equality is achieved if the perturbation field components are proportional to the respective original fields at each detector surface, i.e., $\partial_\theta \boldsymbol{E} = \lambda_i \boldsymbol{E}$, $\partial_\theta \boldsymbol{H} = \lambda_i \boldsymbol{H}$ for all A_i with scalars λ_i. This condition can be met if we interfere the signal with a strong reference beam matching $\partial_\theta \boldsymbol{E}$ at each detector (see Sec. S.1.1 for a detailed consideration of ways how to implement this condition). Henceforth, we refer to the term

$$\boldsymbol{S}^{\mathrm{FI}}(\boldsymbol{r}, t) = 4(\hbar\omega T)^{-1} \int_{t-T/2}^{t+T/2} (\partial_\theta \boldsymbol{E} \times \partial_\theta \boldsymbol{H})(\boldsymbol{r}, \tilde{t})\, \mathrm{d}\tilde{t} \tag{11}$$

as the FI flux. As we are considering quasi-monochromatic waves, the frequency band of the wave is narrow around a frequency ω and can be written as

$$\boldsymbol{E}(\boldsymbol{r}, t) = \mathrm{Re}[\boldsymbol{E}_\omega(\boldsymbol{r}, t)\mathrm{e}^{-\mathrm{i}\omega t}], \tag{12}$$

where $\boldsymbol{E}_\omega$ corresponds to an envelope that varies slowly in time t. If we consider a detector with a measurement time T that is large compared to ω^{-1} but small compared to variations in the envelope, then the highly oscillating contributions are averaged out and the propagation of FI is given by its envelope. This allows us to approximate the FI flux by

$$\boldsymbol{S}^{\mathrm{FI}}(\boldsymbol{r}, t) \approx 2(\hbar\omega)^{-1}\, \mathrm{Re}(\partial_\theta \boldsymbol{E}_\omega^* \times \partial_\theta \boldsymbol{H}_\omega)(\boldsymbol{r}, t). \tag{13}$$

S.1.1 Optimal measurement

In the present analysis, we derived the FI flux assuming a measurement scheme based on photodetectors located in the far field. In order for the photodetectors to reach the limit laid out by the FI flux, the information-carrying part of the wave, $\partial_\theta \boldsymbol{E}_\omega$, needs to match the rest of the outgoing field, $\boldsymbol{E}_\omega$. Following the previously proposed measurement scheme [3], this can be achieved by interfering $\boldsymbol{E}_\omega$ with a strong reference field that is proportional to $\partial_\theta \boldsymbol{E}_\omega$ at each detector surface. Here, we propose ways to implement this requirement with an experimental design based on an array of photodetectors. In this context, it is noteworthy that the FI flux leaving the system not only sets an upper bound on the FI that can be extracted by photodetectors, but on the

FI that can be obtained through any detection scheme of coherent electromagnetic waves under general approximations (see Supplementary Material S.7 for more details).

We take a reference field where the components match the perturbed fields $\partial_\theta \boldsymbol{E}, \partial_\theta \boldsymbol{H}$ up to a multiplicative scalar, i.e., $\partial_\theta \boldsymbol{E} = \lambda_i \boldsymbol{E}, \partial_\theta \boldsymbol{H} = \lambda_i \boldsymbol{H}$. The real constant λ_i is unique for each detector surface A_i over a measurement time T. More specifically, this implies that the reference field and the perturbed field are matched in space, phase, polarization as well as time, at each detector surface A_i and time period T. While these conditions seem very restrictive, we can propose ways to enforce them in practice. In order to fulfill space matching, we can place the detectors far enough away from the scattering region so that the outgoing waves can be approximated as plane waves. If we match the incident angle of the perturbed and reference field on the detector surface, this results in a spatial pattern that is equal between the fields. The phase, on the other hand, can either be matched by hand or by taking a random phase for the reference field, in which case the average FI degrades by a factor of 1/2. By measuring the photons at the photodetectors for two different polarizations independently (e.g., using a polarizing beam splitter), we have a FI that is independent for each polarization allowing us to match the field for each polarization independently. Finally, the quasi-monochromatic field $\partial_\theta \boldsymbol{E}$ has a very slowly varying envelope (compared to the measurement time T); we thus only require a phase-matched monochromatic reference beam at frequency ω for each measurement duration T, which is required to be short compared to the time scale of the envelope function.

S.2 Propagation of information

In this section we show that the Fisher information flux (11) follows a continuity equation while propagating through the system.

We start out by considering solutions $\boldsymbol{E}, \boldsymbol{H}$ to Maxwell's equations with corresponding charges ρ and currents $\boldsymbol{j}$, which depend on a parameter θ. Due to linearity, the fields $\partial_\theta \boldsymbol{E}, \partial_\theta \boldsymbol{H}$ solve Maxwell's equations for the charges $\partial_\theta \rho$ and currents $\partial_\theta \boldsymbol{j}$. The averaged Poynting vector of these fields is proportional to the FI flux, which means that its propagation is described by the averaged Poynting theorem

$$\nabla \cdot \boldsymbol{S}^{\mathrm{FI}} + \partial_t u_{\mathrm{EM}}^{\mathrm{FI}} = -4(\hbar\omega)^{-1} \langle \partial_\theta \boldsymbol{E} \cdot \partial_\theta \boldsymbol{j} \rangle_T, \tag{14}$$

where $u_{\mathrm{EM}}^{\mathrm{FI}} = 2(\hbar\omega)^{-1} \left\langle \epsilon_0 (\partial_\theta \boldsymbol{E})^2 + \mu_0^{-1} (\partial_\theta \boldsymbol{B})^2 \right\rangle_T$ corresponds to the FI density, where the averages are defined as follows: $\langle f \rangle_T(t) = T^{-1} \int_{t-T/2}^{t+T/2} f(\tilde{t})\, \mathrm{d}\tilde{t}$.

S.2.1 Linear macroscopic medium

When a wave enters a linear medium, part of the FI gets deposited in the magnetization and polarization. However, if no losses are present, then this information is extracted when it leaves the medium and returns to free space.

Thus, it is convenient to include these parts in the (total) FI density,

$$u^{\mathrm{FI}} = 2(\hbar\omega)^{-1}\langle \partial_\theta \boldsymbol{E} \cdot \boldsymbol{\epsilon} \partial_\theta \boldsymbol{E} + \partial_\theta \boldsymbol{H} \cdot \boldsymbol{\mu} \partial_\theta \boldsymbol{H} \rangle_T, \tag{15}$$

where the medium is characterized by the static permittivity and permeability tensors, $\boldsymbol{\epsilon}$ and $\boldsymbol{\mu}$, respectively, with constitutive relations $\boldsymbol{D} = \boldsymbol{\epsilon}\boldsymbol{E}$ and $\boldsymbol{B} = \boldsymbol{\mu}\boldsymbol{H}$. With this, we can rewrite the conservation of information in analogy to the conservation of energy as expressed by the Poynting theorem,

$$\nabla \cdot \boldsymbol{S}^{\mathrm{FI}} + \partial_t u^{\mathrm{FI}} = \langle -\partial_\theta \boldsymbol{E} \cdot \boldsymbol{j}^e_{\mathrm{eff}} - \partial_\theta \boldsymbol{H} \cdot \boldsymbol{j}^m_{\mathrm{eff}} \rangle_T. \tag{16}$$

From this expression we can read off that FI is generated by effective electric and magnetic currents:

$$\begin{aligned} \boldsymbol{j}^e_{\mathrm{eff}} &= 4(\hbar\omega)^{-1}[(\partial_\theta \boldsymbol{\epsilon})\partial_t \boldsymbol{E} + \partial_\theta \boldsymbol{j}_f], \\ \boldsymbol{j}^m_{\mathrm{eff}} &= 4(\hbar\omega)^{-1}[(\partial_\theta \boldsymbol{\mu})\partial_t \boldsymbol{H}], \end{aligned} \tag{17}$$

with the current of the free charges given by $\boldsymbol{j}_f$. These effective currents are exclusively located in those areas, where matter changes with the parameter θ, with the interesting consequence that FI is conserved in all other areas of space.

S.2.2 Quasi-monochromatic waves and losses

Here, we consider systems with no free currents and an absorptive linear medium with complex scalars ϵ, μ so that $\boldsymbol{D}_\omega = \epsilon \boldsymbol{E}_\omega$. Associated to the FI flux given in eq. (13) we have a FI density

$$u^{\mathrm{FI}}(\boldsymbol{r}, t) = (\hbar\omega)^{-1}(|\partial_\theta \boldsymbol{E}_\omega|^2 \,\mathrm{Re}[\epsilon] + |\partial_\theta \boldsymbol{H}_\omega|^2 \,\mathrm{Re}[\mu])(\boldsymbol{r}, t). \tag{18}$$

and the FI sources

$$\sigma^{\mathrm{FI}} = -2\hbar^{-1}[\mathrm{Im}(\partial_\theta \boldsymbol{E}^*_\omega \cdot \boldsymbol{E}_\omega \partial_\theta \epsilon) + \mathrm{Im}(\partial_\theta \boldsymbol{H}^*_\omega \cdot \boldsymbol{H}_\omega \partial_\theta \mu)]. \tag{19}$$

Finally, the absorption of energy contributes an additional term, namely

$$\sigma^{\mathrm{abs}} = -2\hbar^{-1}[|\partial_\theta \boldsymbol{E}_\omega|^2 \,\mathrm{Im}(\epsilon) + |\partial_\theta \boldsymbol{H}_\omega|^2 \,\mathrm{Im}(\mu)]. \tag{20}$$

S.2.3 Scattering Matrix

Here, we connect the derivation of the FI in Supplementary Material S.1 and S.2 with the proof given in the main text. We consider monochromatic waves and place a photodetector in the far field of the system with the normal direction $\boldsymbol{n}$ of the detector surface pointing away from the system. This guarantees that the electromagnetic field components are orthogonal to $\boldsymbol{n}$. Then $\langle \cdot, \cdot \rangle$

(given in eq. (7)) turns into an inner product allowing us to construct an orthonormal basis $(\boldsymbol{E}_i, \boldsymbol{H}_i)$ for these states [2, Appendix A]

$$\boldsymbol{E} = \sum_i c_i^d \boldsymbol{E}_i \tag{21}$$

with coefficients c_i^d. If we consider an incident state with coefficients $\boldsymbol{c}^{\text{in}}$ in an arbitrary basis, the scattering matrix $\boldsymbol{S}$ connects the coefficients of the incoming and the outgoing energy flux, which arrives at the detector in the far field, $\boldsymbol{c}^d = \boldsymbol{S}\boldsymbol{c}^{\text{in}}$. In order to find the averaged FI flow we make use of the Hermitian form

$$\frac{1}{2}\sum_i \int_{A_i} \text{Re}(\boldsymbol{E}_\omega^* \times \boldsymbol{H}_\omega) \cdot \text{d}\boldsymbol{n}_i = T^{-1} \langle (\boldsymbol{E}, \boldsymbol{H}), (\boldsymbol{E}, \boldsymbol{H}) \rangle = \boldsymbol{c}^{\text{in}\,\dagger} \boldsymbol{S}^\dagger \boldsymbol{S} \boldsymbol{c}^{\text{in}}, \tag{22}$$

where the left side is the energy flow into the detector for the complex amplitudes $\boldsymbol{E}_\omega, \boldsymbol{H}_\omega$. We want to emphasize here that this relation only depends on the fields $(\boldsymbol{E}, \boldsymbol{H})$ in the vicinity of the detector surfaces. Thus, by letting the system medium depend on θ, the waves entering the detector are still locally solutions to Maxwell's equations. Thus, if the incident state does not change with θ, we see that

$$\begin{aligned} \frac{1}{2}\sum_i \int_{A_i} \text{Re}(\partial_\theta \boldsymbol{E}_\omega^* \times \partial_\theta \boldsymbol{H}_\omega) \cdot \text{d}\boldsymbol{n}_i =& T^{-1} \langle \partial_\theta(\boldsymbol{E}, \boldsymbol{H}), \partial_\theta(\boldsymbol{E}, \boldsymbol{H}) \rangle \\ =& \boldsymbol{c}^{\text{in}\,\dagger} \partial_\theta \boldsymbol{S}^\dagger \partial_\theta \boldsymbol{S} \boldsymbol{c}^{\text{in}}. \end{aligned} \tag{23}$$

S.3 FI radiation patterns

S.3.1 FI radiation of a cube

In this section we consider a weakly scattering ($\epsilon = 1.001\epsilon_0$) cuboid with side lengths L_x, L_y, L_z as depicted in Fig. S1 **a** for $L = L_x = L_y$. Our objective is to estimate the FI radiation pattern corresponding to the position of this cuboid along the z axis, which is the direction of propagation of the incident light field $\boldsymbol{E}_{\omega,0}(\boldsymbol{r}) = \boldsymbol{E}_0 \exp(\text{i}kz)$, with the field being linearly polarized in y-direction. Our scheme allows us to identify the sources of FI located at the front and back side of the cuboid. Using the free space dyadic Green's function G_ω, we can approximate

$$\partial_\theta \boldsymbol{E}_\omega(\boldsymbol{r}) \propto \int G_\omega(\boldsymbol{r}, \boldsymbol{r}')(\boldsymbol{j}_{\text{eff}}^e)_\omega(\boldsymbol{r}')\,\text{d}\boldsymbol{r}' \tag{24}$$

and similarly

$$(\boldsymbol{j}_{\text{eff}}^e)_\omega(\boldsymbol{r}') \approx -4\text{i}\hbar^{-1} \boldsymbol{E}_{\omega,0}(\boldsymbol{r}') \partial_\theta \epsilon(\boldsymbol{r}'). \tag{25}$$

In the far field $|\boldsymbol{r}| \gg |\boldsymbol{r}'|$ the Green's function simplifies in the lowest order to

$$G_\omega(\boldsymbol{r}, \boldsymbol{r}') \approx G_\omega(\boldsymbol{r}, 0) e^{-ik\hat{\boldsymbol{r}}\cdot\boldsymbol{r}'}, \tag{26}$$

where $\hat{\boldsymbol{r}}$ is the unit vector pointing in the direction of $\boldsymbol{r}$. Finally we can also approximate the following Poynting like vector associated to the Green's function in the far field

$$\frac{1}{2\omega}\,\mathrm{Im}((G_\omega(\boldsymbol{r},0)\boldsymbol{E}_0)^*\times(\nabla\times(G_\omega(\boldsymbol{r},0)\boldsymbol{E}_0))\approx\frac{1}{2\omega}\frac{k}{(4\pi r)^2}[1-\hat{\boldsymbol{r}}_y^2]|\boldsymbol{E}_0|^2,\quad(27)$$

which corresponds to the radiation pattern of a short dipole antenna. Using these approximations, it is easy to show that the far-field FI radiation pattern is given by

$$\boldsymbol{S}^{\mathrm{FI}}(\boldsymbol{r})\propto\hat{\boldsymbol{r}}[1-\hat{\boldsymbol{r}}_y^2]\begin{cases}\sin^2(\frac{k\hat{\boldsymbol{r}}_xL_x}{2})\,\mathrm{sinc}^2(\frac{k\hat{\boldsymbol{r}}_yL_y}{2})\,\mathrm{sinc}^2(\frac{k(1-\hat{\boldsymbol{r}}_z)L_z}{2}), & \theta=x_{\mathrm{scat}},\\ \mathrm{sinc}^2(\frac{k\hat{\boldsymbol{r}}_xL_x}{2})\,\sin^2(\frac{k\hat{\boldsymbol{r}}_yL_y}{2})\,\mathrm{sinc}^2(\frac{k(1-\hat{\boldsymbol{r}}_z)L_z}{2}), & \theta=y_{\mathrm{scat}},\\ \mathrm{sinc}^2(\frac{k\hat{\boldsymbol{r}}_xL_x}{2})\,\mathrm{sinc}^2(\frac{k\hat{\boldsymbol{r}}_yL_y}{2})\,\sin^2(\frac{k(1-\hat{\boldsymbol{r}}_z)L_z}{2}), & \theta=z_{\mathrm{scat}}.\end{cases}\quad(28)$$

The $\mathrm{sinc}(x)=\sin(x)/x$ functions result from the interference of the sources within each side of the scatterer, respectively. On the other hand, the sin term is due to the interference of the two sources with each other. Finally, the term $[1-\hat{\boldsymbol{r}}_y^2]$ corresponds to the scattering limitations due to the polarization of the incident field in accordance with the dyadic Green's function (The dipoles of the effective currents oscillate parallel to the incident field, which suppresses dipole radiation in the polarisation direction).

We will now use this formula to explain the FI radiation patterns of cuboid particles, which will give us an understanding on some of the main features to expect for the FI radiation pattern of more general particle shapes such as spheres. We start out by considering the displacement of a cuboid ($L=L_x=L_y$) along the x direction (see Fig. S1**a**). In this case, the $\mathrm{sinc}^2(k\hat{\boldsymbol{r}}_yL/2)$ function guarantees that the intensity is focused along directions $\hat{\boldsymbol{r}}$ on the x-z plane (i.e. $\hat{\boldsymbol{r}}_y\approx 0$). Similarly, the interference of the sources along the z axis results in the term $\mathrm{sinc}^2(k(1-\hat{\boldsymbol{r}}_z)L_z/2)$, which guarantees that $\hat{\boldsymbol{r}}_z\approx 1$. However, no radiation occurs in the exact forward direction $\hat{\boldsymbol{r}}=\boldsymbol{e}_z$ due to the factor $\sin^2(k\hat{\boldsymbol{r}}_xL/2)$ becoming zero in that case. Furthermore, due to $\hat{\boldsymbol{r}}_z\approx\sqrt{1-\hat{\boldsymbol{r}}_x^2}\approx 1-\hat{\boldsymbol{r}}_x^2/2$, we can see that $\hat{\boldsymbol{r}}_z$ is changing only slowly for small $\hat{\boldsymbol{r}}_x$. Therefore, the main variations of the radiation patterns (given by $\sin^2(k\hat{\boldsymbol{r}}_xL_x/2)$) are caused by the interference of the sources located at the left and right side of the cube, creating a radiation pattern similar to a double slit experiment. However, while for the double slit experiment the number of visible peaks is limited by the width of the double slit, in our case we are limited by the interference of the sources along the z direction as can be seen in the right panels of Fig. S1**a**. As we decrease the length L_z of the cuboid along the z direction, the remaining sources along the z direction are more closely aligned. This reduces the destructive interference of the radiated information, especially along steeper angles (i.e. $|\hat{\boldsymbol{r}}_x/\hat{\boldsymbol{r}}_z|>1$), so that more peaks become visible.

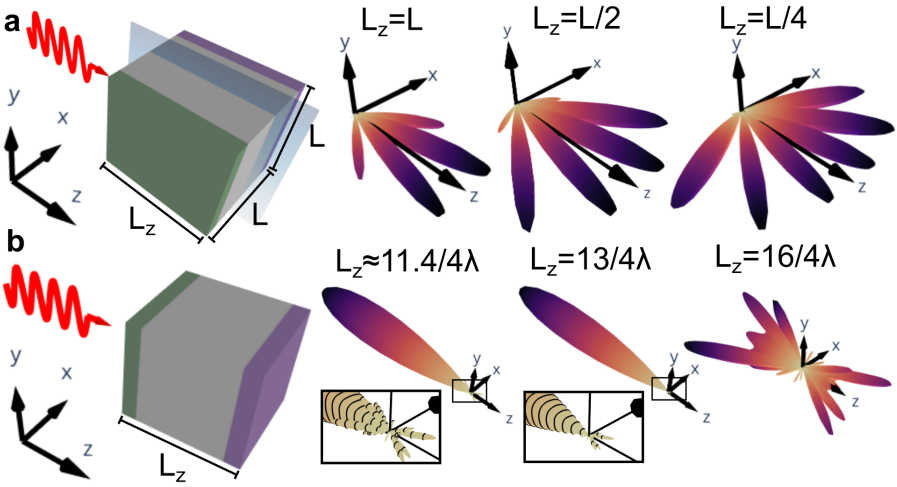

Fig. S1 FI radiation pattern of a weakly scattering cuboid. a, (Left panel) Sketch of a cuboid dielectric (side length L along x, y direction, L_z along z direction, refractive index $n = 1.001$) illuminated by a plane wave moving along the z axis (wavelength $\lambda = R/0.7$). With the parameter of interest being the target's position along the x direction, the FI sources are located at the two corresponding sides (green for negative $\partial_\theta \epsilon$; purple for positive $\partial_\theta \epsilon$). The symmetry plane in blue results in the suppression of the FI radiation patterns along the plane's tangential directions (see Sec. S.3.4). (Right panels) We vary the length L_z of the cuboid along the z direction. By reducing the length L_z, the remaining sources located along the z direction are more closely aligned in phase, which reduces their destructive interference, thus making more lobes in the FI radiation pattern visible. **b**, (Left panel) A cuboid with the parameter of interest being the cuboid's position in z direction. (Right panels) We vary the length of the cuboid along the z direction. Starting from $L_z = L \approx 11.4/4\lambda$, we can see that the main peak of the radiation pattern increases compared to the smaller peaks (see insets with black contour lines being included for better visualization), up to the point where the dimensions are such that the sources positively interfere for back-reflected waves ($L_z = 13/4\lambda$). On the other hand, we can choose the length L_z such that the back-reflected information destructively interferes, making only the secondary peaks visible ($L_z = 16/4\lambda$).

On the other hand, if we instead consider the case of $\theta = z_{\text{scat}}$ as depicted in Fig. S1**b**, then the two sources behave similarly to two rectangular aperture antennas [4]. The interference pattern given by $\text{sinc}^2(k\hat{\boldsymbol{r}}_x L/2)\,\text{sinc}^2(k\hat{\boldsymbol{r}}_y L/2)$ is induced by the interference of the sources along the x and y direction. The phase differences of the sources along the z direction result in the term $\sin^2(k(1-\hat{\boldsymbol{r}}_z)L_z/2)$ suppressing forward scattering. Similar to before, we can see that $\hat{\boldsymbol{r}}_z = \sqrt{1-\hat{\boldsymbol{r}}_x^2-\hat{\boldsymbol{r}}_y^2} \approx 1-(\hat{\boldsymbol{r}}_x^2+\hat{\boldsymbol{r}}_y^2)/2$, showing that $\hat{\boldsymbol{r}}_z$ only changes slowly with perturbations of $\hat{\boldsymbol{r}}_x, \hat{\boldsymbol{r}}_y$. Thus, the oscillations of $\sin^2(k(1-\hat{\boldsymbol{r}}_z)L_z/2)$ are only visible in the side peaks of the sinc^2 functions. In the right panels of Fig. S1**b** we consider this more closely by varying the length of the cuboid along the z direction. For $L_z = L \approx 11.4/4\lambda$ we can see that the information is almost exclusively radiated in backwards direction. The other peaks (see inset) are strongly suppressed due to the secondary peaks of the sinc^2 functions being comparatively low in amplitude. This is even more pronounced if we choose

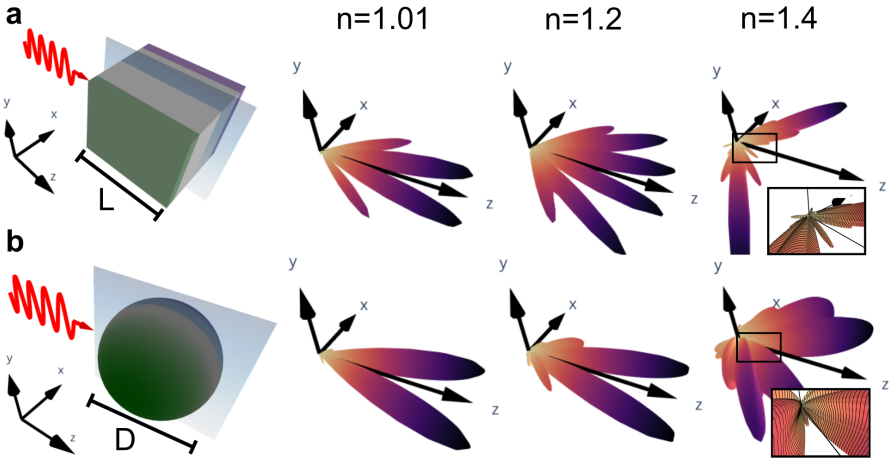

Fig. S2 FI radiation patterns and refractive index. We consider the FI radiation patterns in **a** for a cube (side length $L = \lambda/0.35$) and in **b** for a sphere (diameter $D = \lambda/0.35$) illuminated by an incident Gaussian beam (NA $= 0.1$, wavelength λ) for different scatterer refractive indices (see values of n indicated on the top). The parameter of interest is the position of the scatterers along the x axis.

the length $L_z = 13/4\lambda$ (i.e. $kL_z = l\pi + \pi/2$; $l = 6$ chosen for higher numerical stability), such that the back-reflected information constructively interferes. By comparing the insets, we see that the ratio of the secondary peaks compared to the main peak is considerably smaller for $L_z = 13/4\lambda$ than for $L_z = L$. On the contrary, for $L_z = 16/4\lambda$ (i.e. $kL_z = 8\pi$) we get perfect destructive interference of the FI radiation in the backward direction, such that the main peak of the sinc^2 functions is suppressed, making the secondary peaks clearly visible.

Finally, it should be noted that for both the double slit and the rectangular aperture, the radiation pattern of energy flux is commonly calculated by the introduction of effective electric and magnetic currents [4] located at the apertures. This can be directly compared to our result where we describe the radiation of FI using only effective electric currents located at the sides of the cube. The absence of the magnetic current enters Eq. (28) in the prefactor $[1 - \hat{\boldsymbol{r}}_y^2]$, which suppresses the field along the polarization direction of the electric field compared to the prefactor $[1 + \hat{\boldsymbol{r}}_z]^2$ for scattering at an aperture, which suppresses the back-reflection of the field.

S.3.2 FI radiation patterns and refractive index

In order to get an understanding on how the refractive index influences the FI radiation patterns, we first consider a cube with side length $L = \lambda/0.35$ given in Fig. S2**a**. For the case of a near free space dielectric constant (refractive index $n = 1.001$), the information is primarily radiated in forward direction. While the radiation in direct transmission is suppressed due to the destructive

interference of the sources on the sides, the destructive interference of the sources along the z direction suppresses peaks with larger angles (i.e. $|\hat{\boldsymbol{r}}_x/\hat{\boldsymbol{r}}_z| > 1$). Increasing the refractive index ($n = 1.2$), we observe a reduction of the destructive interference so that more peaks become visible. Furthermore, the increased refraction and phase accumulation of the light while traversing the scatterer decreases the angular separation of the lobes and effectively moves the peaks closer to the z axis. Increasing the refractive index further to $n = 1.4$ shows that the first forward peaks move even closer to the z axis and are strongly suppressed (see inset).

We now shift our focus to a spherical particle with diameter $D = \lambda/0.35$. The corresponding radiation patterns are shown in Fig. S2**b**. For a dielectric constant close to that of vacuum (refractive index $n = 1.001$), the information is almost exclusively radiated along two forward lobes. This is consistent with the observation that the sources of the sphere can be viewed as a sequence of bent double slits. The average distance between the slits is reduced compared to the case of the cube, which broadens the peaks moving the secondary lobes to the sides and effectively decreasing them in size. When increasing the refractive index, we can see that again the destructive interference is reduced, revealing secondary lobes. Finally, similar to the cube, the forward lobes move towards the z axis and the first pair of forward lobes are strongly suppressed (see inset).

S.3.3 Information radiation in forward scattering direction

Here, we consider arbitrarily shaped scatterers, for which we want to estimate the overall center of mass position $\boldsymbol{r}$. The scattering matrix $\boldsymbol{S}$ connects the amplitudes $\boldsymbol{c}^{\text{in}}$ of the incident plane waves centered at an arbitrary location $\boldsymbol{r}_0$ with k-vectors $\boldsymbol{k}^{\text{in}}$ with the amplitudes of the outgoing plane waves $\boldsymbol{c}^{\text{out}}$ also centered at $\boldsymbol{r}_0$ with $\boldsymbol{k}^{\text{out}}$ by

$$c^{\text{out}}_{\boldsymbol{k}^{\text{out}}} = S_{\boldsymbol{k}^{\text{out}},\boldsymbol{k}^{\text{in}}} c^{\text{in}}_{\boldsymbol{k}^{\text{in}}}. \tag{29}$$

If we consider the case where we want to estimate a particle's position along a given direction $\Delta\boldsymbol{r}$, in free space parameterized by θ, then instead of shifting the center of mass of the particle $\boldsymbol{r}$, we can equivalently shift the incoming plane waves in the opposite direction. For the coefficients this results in the relation

$$c^{\text{out}}_{\boldsymbol{k}^{\text{out}}} \exp\big(-\mathrm{i}\theta \boldsymbol{k}^{\text{out}} \cdot \Delta\boldsymbol{r}\big) = S_{k^{\text{out}},\boldsymbol{k}^{\text{in}}}(\theta) c^{\text{in}}_{\boldsymbol{k}^{\text{in}}} \exp\big(-\mathrm{i}\boldsymbol{k}^{\text{in}} \cdot \Delta\boldsymbol{r}\theta\big), \tag{30}$$

and gives us direct insight on how the scattering matrix changes with the parameter θ:

$$S_{k^{\text{out}},\boldsymbol{k}^{\text{in}}}(\theta) = S_{k^{\text{out}},\boldsymbol{k}^{\text{in}}}(0) \exp\big(\mathrm{i}(\boldsymbol{k}^{\text{in}} - \boldsymbol{k}^{\text{out}}) \cdot \Delta\boldsymbol{r}\theta\big). \tag{31}$$

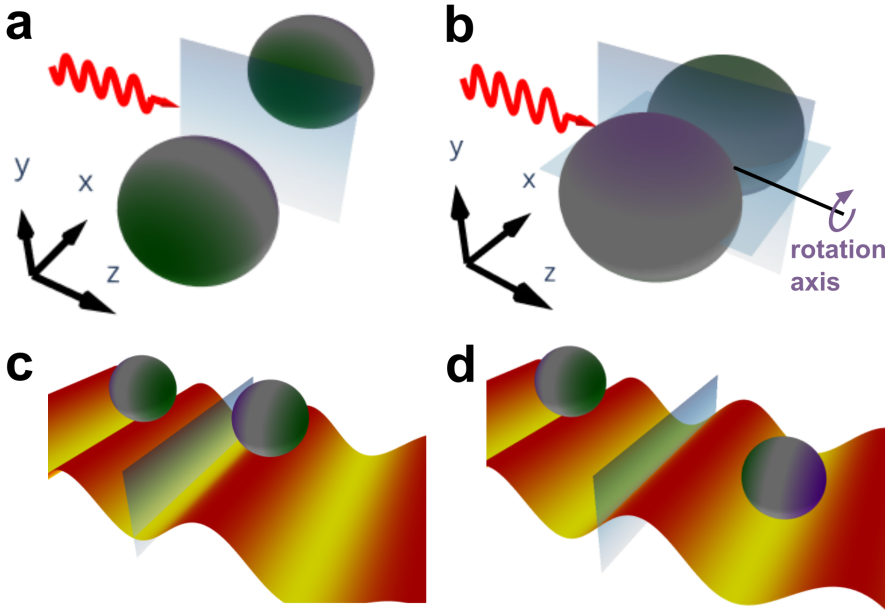

Fig. S3 Symmetries and FI radiation patterns. a, Two particles located along the x axis illuminated by a plane wave (red curve), with the center of mass motion along the x direction as the parameter of interest. The reflection anti-symmetry of the FI sources with respect to the blue plane results in no information being radiated along the tangential directions. **b**, Rotation of a dumbbell shaped particle around the propagation axis of the incident field. In **c** and **d** we look at two particles illuminated by a standing wave (red-yellow surface). If the particles are situated at anti-nodes with the same phase (**c**) or a π phase shift (**d**), then the information radiation on their center of mass motion (**c**) or their relative motion along the direction of the standing wave (**d**), respectively, is suppressed along the symmetry plane (blue surface).

Correspondingly, we arrive at the following relation for the radiation pattern of the system for plane wave illumination:

$$4|\partial_\theta S_{\boldsymbol{k}^{\rm out},k^{\rm in}}|^2\Big|_{\theta=0} = 4|(\boldsymbol{k}^{\rm out}-\boldsymbol{k}^{\rm in})\cdot\Delta\boldsymbol{r}|^2|S_{\boldsymbol{k}^{\rm out},\boldsymbol{k}^{\rm in}}|^2, \tag{32}$$

which describes the FI that propagates in the direction of $\boldsymbol{k}_{\rm out}$, when the target is illuminated with a plane wave with wave vector $\boldsymbol{k}_{\rm in}$. An important consequence of this relation is that there will never be any information scattered in the direct forward direction for plane wave illumination. Similarly, if $\boldsymbol{k}^{\rm out},\boldsymbol{k}^{\rm in}$ lie in the plane orthogonal to $\Delta\boldsymbol{r}$, then we have $|(\boldsymbol{k}^{\rm out}-\boldsymbol{k}^{\rm in})\cdot\Delta\boldsymbol{r}|^2=0$. This implies that no information is radiated towards $\boldsymbol{k}^{\rm out}$. These insights are applicable to very general particle shapes and thus could prove to be an important tool for deciding where to place detectors to optimally collect the information in corresponding experiments.

S.3.4 FI radiation limited by system symmetries

Using the symmetries of the system makes it possible to find constraints on the radiation of FI due to destructive interference along spherical angles lying on the corresponding symmetry plane. To see this, we consider a dielectric particle with the FI getting induced by the effective electric current (see eq. (17))

$$(\boldsymbol{j}^e_{\text{eff}})_\omega(\boldsymbol{r}) \propto \boldsymbol{E}_\omega(\boldsymbol{r})\partial_\theta\epsilon(\boldsymbol{r}). \tag{33}$$

In general, if the incident field and the dielectric are both reflection symmetric with respect to a given plane (see Fig. 3**b**) then the field $\boldsymbol{E}_\omega(\boldsymbol{r})$ preserves this symmetry. This means that if $\partial_\theta\epsilon$ is anti-symmetric with respect to the same plane, then so is $(\boldsymbol{j}^e_{\text{eff}})_\omega$ and thus $\partial_\theta\boldsymbol{E}_\omega$. Consequently, no FI can be radiated along the tangential components of the plane (see Fig. 3**b**). This even holds for a multi-particle system such as two particles located along the x axis that are being illuminated by a plane wave (see Fig. S3**a**). In this case, the radiated information on the center of mass motion of the two-particle system is suppressed along the indicated symmetry plane (blue plane), showing that no information on this motion is present in the back-reflection and the forward scattering direction (see Eq. (32)). Another noteworthy case is that of rotational degrees of freedom as shown in Fig. S3**b**. Here, a "dumbbell"-shaped particle, constructed by connecting two spheres, is rotating around the axis of propagation of the light field. In this case, two symmetry planes are present, which suppress the outgoing FI along these directions.

Finally, we consider the case of two particles located inside of a standing wave (see Fig. S3**c**,**d**). When the particles are located on two anti-nodes with the same phase of the standing wave, then this wave is symmetric with respect to the indicated plane in blue. This results in the information of the center of mass motion in the direction of the standing wave being suppressed along the plane's tangents. On the other hand, for particles situated at the anti-nodes with a π phase difference, the standing wave is anti-symmetric with respect to the depicted plane. Thus, the relative motion of the particles is suppressed instead. This highlights the importance of the placement of particles in relation to each other inside of multi-particle trapping fields.

S.4 Hiding information from an eavesdropper

Here, we show that despite the structural similarity between the Poynting theorem and the FI continuity equation, it would be misleading to assume that the flow of energy and the flow of information exhibit analogous behavior for any given wave field. We exploit this to simulate a system in which electromagnetic energy is transmitted with high efficiency, while the Fisher information is back-reflected to the source of the probing wave, effectively hiding it from a potential eavesdropper in transmission direction. For this purpose, we open up the left side of the waveguide shown in Fig. 2 and add 25 circular scatterers to the left of the target in our simulations. (For the full geometry see Sec. S.4.1.) Previously, we made use of the FI operator $\boldsymbol{F}$ to identify the incident state

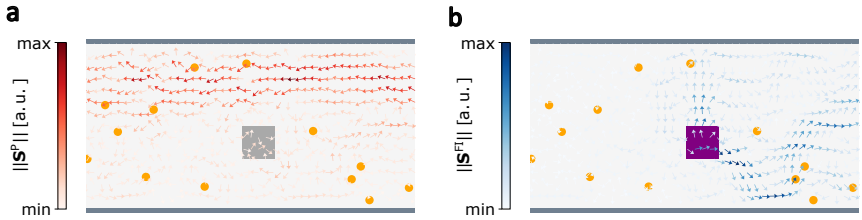

Fig. S4 Comparison of Fisher information and energy flow. Simulated Poynting vector field (red arrows in **a**), and Fisher information flux (blue arrows in **b**) around the target scatterer (refractive index $n = 1.44$) at $f = 11.8$ GHz, when injecting an incident state that maximizes the Fisher information ratio between the transmission and reflection channels. With the estimation parameter θ of interest being here the target scatterer's refractive index, the FI sources are located in its entire area (purple square in **b**). Both the target scatterer and the disorder (orange circles) have a refractive index of $n = 1.44$. We observe that while almost all (96.3%) of the wave's energy is transmitted to the left (see **a**), almost all (98.4%) of the Fisher information is flowing to the opposite direction (to the right, see **b**).

that transmits the highest FI to the far field. By taking the FI matrices $\boldsymbol{F}_L$ and $\boldsymbol{F}_R$, corresponding to the FI available at the left and right waveguide lead, respectively, we construct the following operator, $\boldsymbol{F}^{\mathrm{rel}} = (\boldsymbol{F}_R + \boldsymbol{F}_L)^{-1}\boldsymbol{F}_L$. This "relative FI operator" allows us to identify the state that maximizes the ratio between the information received at the right and the left lead (see Sec. S.4.2 for further details).

In Fig. S4**a**, we show the eigenstate of this operator that corresponds to the maximal eigenvalue. The corresponding state features a Poynting vector field (red arrows), which can be seen to follow a pattern of strong transmission from right to left along the top of the waveguide. On the contrary, Fig. S4**b** shows that the FI flux is flowing to the right side of the waveguide and thus in the opposite direction to the dominant flow of energy in this system. This not only highlights that the FI flux and the Poynting vector represent distinct concepts, but also that we can collect information about a parameter at a detector (located in the right lead), with very little loss of information to a potential eavesdropper (assumed here to be located in the left lead).

S.4.1 Numerics of 2D waveguide simulations

As described in Methods Sec. M.1.2, only the lowest transverse mode is open between the top and the bottom plate of the experimental setup in the considered frequency range. Therefore, the z-component of the electric field does not depend on the z-coordinate, and we obtain it numerically by solving the 2D Helmholtz equation

$$\left(\triangle + n^2(x,y)k_0^2\right)\psi(x,y) = 0, \tag{34}$$

using the finite-element library NGSolve [5]. In Eq. (34), $\triangle$ denotes the Laplace operator, $n(x,y)$ the position-dependent refractive index, $k_0 = \frac{2\pi}{\lambda}$ the vacuum wavenumber, and $\psi(x,y)$ the z-component of the electric field. We

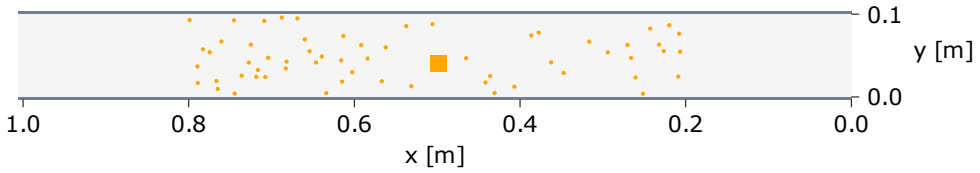

Fig. S5 Simulated 2D geometry with two open leads: While the system is subject to Dirichlet boundary conditions at the top and the bottom side, it is infinitely long in x-direction. We hide a square Teflon target within a complex scattering layer of 60 circular Teflon scatterers and probe the system by injecting microwaves from the right side.

apply Dirichlet boundary conditions at the waveguide plates, and use perfectly matched layers to implement an infinitely extended system in x-direction. To account for the experimental losses due to the skin effect, we add an imaginary part of 10^{-3} i to the refractive index of the entire system.

We apply this framework to simulate a waveguide with two open leads in Fig. S4. While we use the 2D projection of the experimental scattering geometry on the right side of the target, we place 35 additional Teflon scatterers on its left, see Fig. S5. We choose 2 cm for the side length of the square target and 2.55 mm for the radius of the circular scatterers in the disorder. Note that, unlike in the experiment, Teflon is used as the material of the target.

S.4.2 The relative FI operator

To motivate and derive the aforementioned relative Fisher information operator, we consider the scenario where we gather information about the system through a receiver while trying to avoid that this information ends up at a potential eavesdropper. More specifically, we want to find an incident field for which the ratio of the FI rates $\mathcal{J}_R/\mathcal{J}_E$ is maximized, where $\mathcal{J}_R, \mathcal{J}_E$ are the rates of FI of the receiver and eavesdropper, respectively. This problem is equivalent to maximizing the relative FI of the receiver lead $\mathcal{J}_R/(\mathcal{J}_E + \mathcal{J}_R)$, which is numerically more stable and therefore our method of choice. To show the equivalence, we define $\mathcal{J}_R/\mathcal{J}_E = \beta > 0$ and with this rewrite $\mathcal{J}_R/(\mathcal{J}_E+\mathcal{J}_R) = \beta/(1+\beta) = f(\beta)$, where $f(\beta)$ is monotonically increasing for $\beta > 0$, guaranteeing that the two expressions are maximized simultaneously. We start out by splitting the space of outgoing waves into two orthogonal subspaces of dimensions M_R (at the receiver end) and M_E (at the eavesdropper's end). We use the scattering matrices $\boldsymbol{S}_R, \boldsymbol{S}_E$, which describe the scattering of the incident wave into the outgoing waves at the receiver and eavesdropper's end to define the FI operators $\boldsymbol{F}_R, \boldsymbol{F}_E$ on these subspaces, respectively [3]. We can reformulate the problem to

$$\max_{\boldsymbol{c}^{\text{in}}} \frac{[\boldsymbol{c}^{\text{in}}]^\dagger \boldsymbol{F}_R \boldsymbol{c}^{\text{in}}}{[\boldsymbol{c}^{\text{in}}]^\dagger (\boldsymbol{F}_R + \boldsymbol{F}_E) \boldsymbol{c}^{\text{in}}}, \tag{35}$$

where the vector $\boldsymbol{c}^{\text{in}}$ indicates the incident wave. Due to the matrices being Hermitian and positive definite, we can use the matrices in the denominator

to define an inner product $\langle \boldsymbol{c}, \boldsymbol{d} \rangle = \boldsymbol{c}^\dagger (\boldsymbol{F}_R + \boldsymbol{F}_E)\boldsymbol{d}$ on the incident states. We rewrite the optimization problem eq. (35) to

$$\max_{\boldsymbol{c}^{\text{in}}} \frac{\left\langle \boldsymbol{c}^{\text{in}}, (\boldsymbol{F}_R + \boldsymbol{F}_E)^{-1} \boldsymbol{F}_R \boldsymbol{c}^{\text{in}} \right\rangle}{\left\langle \boldsymbol{c}^{\text{in}}, \boldsymbol{c}^{\text{in}} \right\rangle}. \tag{36}$$

The operator $(\boldsymbol{F}_R + \boldsymbol{F}_E)^{-1}\boldsymbol{F}_R$ is self-adjoint with respect to this inner product, allowing us to apply the min-max theorem, which states that eq. (36) is maximized for the eigenstate corresponding to the largest eigenvalue. Due to the signal being prone to noise for waves which avoid the target, it can be beneficial to exclude waves with $[\boldsymbol{c}^{\text{in}}]^\dagger (\boldsymbol{F}_R + \boldsymbol{F}_E)\boldsymbol{c}^{\text{in}} < \epsilon$ for some cutoff ϵ. This can be achieved by applying an orthogonal projection on both sides of the FI matrices $\boldsymbol{F}_R, \boldsymbol{F}_E$.

S.5 FI of a weak detector in the near field

In this section, we consider a weak detector, which measures the field at any given location (even inside of the system). For this, we consider the ionization process of an atom, where the FI stored in the electromagnetic field is transferred to the ionization process of the atom. With the source of the noise being the quantum nature of our system, we need to view the interaction between the atom and the field from a quantum mechanical perspective. If the electromagnetic field is not too weak, then the system can be described semi-classically and over long enough time scales we can further use the rotating wave approximation to describe the ionization process of an electron. We start with an atom with a bounded electron with the corresponding ground state energy E_0 at time t_0 getting ionized toward the continuum energy $E = E_0 + \hbar\omega$ due to a quasi-monochromatic field at frequency ω. The probability p that a transition has taken place during the time interval Δt is given to first order in time by (valid for $p \ll 1$) [6]

$$p \approx 2\eta_0 \frac{u_{E^T}}{\hbar\omega} \Delta t, \tag{37}$$

for the detection efficiency η_0 of the atom and the transverse electric energy density $u_{E^T} = \epsilon_0 |\boldsymbol{E}_\omega^T|^2/4$. It is important to note that the atom's dipole only interacts with the transverse part of the electric field. This is encapsulated in the electric dipole Hamiltonian, which only contains the transverse part of the magnetic vector potential, guaranteeing gauge invariance [6]. Furthermore, the detection efficiency has a dependence on the polarization of the light relative to the orientation of the dipole. In order to average out this degree of freedom, we now consider a system made up of N atoms located in the immediate vicinity of the location $\boldsymbol{r}_0$ with random orientations. For each atom i the ionization probability within a time interval $[0, \Delta t]$ can be described by a Bernoulli distribution with respective probability p_i. We denote the ionization probability averaged over all atoms by $\overline{p}$. We can now see that the rate of energy transfer ΔE from the electromagnetic field toward the electrons is

proportional to the transverse electric energy density u_{E^T},

$$\Delta E = N\overline{p}\hbar\omega \approx 2N\eta u_{E^T}\Delta t, \tag{38}$$

where η represents the averaged detection efficiency.

In order to derive the corresponding transfer of FI in this process, we assume that the ionization events of the individual atoms are independent of each other. Thus, we can make use of Le Cam's theorem for $\overline{p^2} \ll N^{-1}$, which tells us that we can approximate the number of measured photo-electrons within the time interval Δt by a Poisson distribution $P(N\overline{p})$ [7]. With this we can write for the FI contained in the ionization process in a given time interval $[0, \Delta t]$,

$$\mathcal{F}_e(\theta) \approx \frac{[N\partial_\theta \overline{p}]^2}{N\overline{p}} \leq 2N\eta u^{\mathrm{FI}}_{E^T}\Delta t, \tag{39}$$

where the FI density in the transverse electric field is given by $u^{\mathrm{FI}}_{E^T} = (\hbar\omega)^{-1}\epsilon_0|\partial_\theta \boldsymbol{E}^T_\omega|^2$. The inequality is due to Cauchy-Schwartz, where equality is saturated in the case where all the changes of the field with θ are contained within the amplitude of the field (and not in the phase) and are thus visible in the ionization rate (i.e., $\partial_\theta \boldsymbol{E}^T_\omega = \lambda \boldsymbol{E}^T_\omega$ with a real scalar λ). The right side also corresponds to the limit that can be achieved if we measure the ionization process of each atom independently. This shows that measuring the total count of photo-electrons is sufficient to access the overall FI from the individual ionization processes.

Overall, eq. (39) shows that extraction of FI out of the field is governed by the transverse electric field part of the FI density in the same way as the transverse electric field part of the energy density determines the transfer of energy toward the electrons. This result corroborates the notion that the FI density introduced here is, indeed, a measure of the local FI content of the electromagnetic field.

S.6 FI density in close proximity to matter

Matter and charged particles produce longitudinal electric fields in their surroundings. Take for example a charged particle, which creates a longitudinal electric field

$$\boldsymbol{E}^L = \frac{1}{4\pi\epsilon_0}\frac{q}{r^2}\hat{\boldsymbol{r}}, \tag{40}$$

where $\hat{\boldsymbol{r}}$ is the unit vector in the direction of $\boldsymbol{r}$. While the electric field strength decays quadratically with distance, $|\boldsymbol{E}^L| \propto r^{-2}$, the FI density corresponding to the particle position decays much more strongly: $u^{\mathrm{FI}}_{E^L} \propto |\partial_\theta \boldsymbol{E}^L|^2 \propto r^{-6}$. This can even be extended to more complex systems made up of matter described by a current $\boldsymbol{j}$ and a charge density ρ. More specifically, for the longitudinal part of the electric field we can rewrite the Ampère-Maxwell equation,

$$\epsilon_0 \partial_t \boldsymbol{E}^L = \boldsymbol{j}^L, \tag{41}$$

where the longitudinal current $\boldsymbol{j}^L$ can be written as [8],

$$\boldsymbol{j}^L(\boldsymbol{r},t) = \frac{1}{3}\boldsymbol{j}(\boldsymbol{r},t) + \frac{1}{4\pi}P\int \frac{\mathbf{1}-3\hat{\boldsymbol{R}}^T\hat{\boldsymbol{R}}}{R^3}\boldsymbol{j}(\boldsymbol{r}',t)\,\mathrm{d}^3\boldsymbol{r}'. \tag{42}$$

Here P refers to the Cauchy principal value (with spherical contraction) and $\boldsymbol{R} = \boldsymbol{r} - \boldsymbol{r}'$. Importantly, this means that the longitudinal current $\partial_\theta \boldsymbol{j}^L$ is localized near the matter, giving us the following scaling in the distance $\tilde{r}$ to the closest part of matter:

$$\partial_\theta \boldsymbol{j}^L(\boldsymbol{r},t) = \mathcal{O}(\tilde{r}^{-3}). \tag{43}$$

Plugging this into eq. (41) provides us with the scaling for the FI density

$$u^{\mathrm{FI}}_{E^L_\omega} \propto |\partial_\theta \boldsymbol{E}^L_\omega|^2 = \mathcal{O}(\tilde{r}^{-6}). \tag{44}$$

This shows that in the semi-classical case the FI that can be extracted out of the system by the described photodetectors is locally given by the transverse electric part of the FI density except in areas in very close proximity to matter. On the other hand, even in these areas the FI density sets an upper bound to the extractable FI and accounts for the FI that is temporarily stored inside the longitudinal components of the electric field (e.g. in the polarization of the matter, in the longitudinal components at the given frequency, etc.).

S.7 Optimality of the FI density

In sections S.1 and S.2 we have shown that the total amount of FI that can be extracted in the far field with photodetectors is given by the FI density. Here we will see that the integrated FI density not only represents a limit for photodetectors, but for any measurement device (not in close proximity to matter), extending previous results [3], which showed that the Quantum Fisher information (QFI) $\mathcal{I}$ leaving the system can be reached using only photodetectors. To this end, we consider the QFI of a quasi-monochromatic coherent photon state, which corresponds to the maximum amount of FI that can be extracted out of a state with any measurement scheme. With the calculation of the QFI requiring a quantum description of the system, we need to quantize the electromagnetic field. The starting point is to consider a free electromagnetic field, which displays the behaviour of the QFI in regions sufficiently distant from matter. We show that the spatially integrated FI density yields the QFI of the system. Finally, we derive the same result when adding macroscopic matter and neglecting the interaction of the detector with the field and using the rotating wave approximation.

S.7.1 QFI of the Free Electromagnetic Field

The Hamiltonian for a free transversal electromagnetic field is given by

$$\hat{H}_{\mathrm{em}} = \frac{1}{2}\int \epsilon_0(\hat{E}^T)^2 + \mu_0^{-1}\hat{B}^2\,\mathrm{d}\boldsymbol{r} = \int \hbar\omega(k)\left(\hat{a}_{\boldsymbol{k}}^\dagger \hat{a}_{\boldsymbol{k}} + \frac{1}{2}\right)\mathrm{d}\boldsymbol{k} \tag{45}$$

with the transverse field operators $\hat{E}^T$ and $\hat{B}$ and the photon annihilation operators $\hat{a}_{\boldsymbol{k}}$ in the representation of the wave vectors $\boldsymbol{k}$, where we omitted the polarization index for simpler notation. As a first step, we consider a system made up of electromagnetic waves in vacuum and calculate the QFI contained in the state of the system. In order to connect the QFI with the FI density, we introduce the operator

$$\hat{K} = \int \epsilon_0(\hat{E}^T)^-(\hat{E}^T)^+ + \mu_0^{-1}\hat{B}^-\hat{B}^+\,\mathrm{d}\boldsymbol{r}, \tag{46}$$

where $(\hat{E}^T)^+/(\hat{E}^T)^-$ corresponds to the positive/negative frequency part of the transverse part of the electric field operator and correspondingly for $\hat{B}$. Using the quantization of the electromagnetic field from eq. (45), we thus get

$$\hat{K} = \int \hbar\omega(k)\hat{a}_{\boldsymbol{k}}^\dagger \hat{a}_{\boldsymbol{k}}\,\mathrm{d}\boldsymbol{k}. \tag{47}$$

For a coherent quasi-monochromatic state with frequency ω given by the amplitude $\boldsymbol{\alpha}$ we thus get

$$\langle\boldsymbol{\alpha}|\hat{K}|\boldsymbol{\alpha}\rangle = \frac{1}{4}\int \epsilon_0|\boldsymbol{E}_\omega^T|^2 + \mu_0^{-1}|\boldsymbol{B}_\omega|^2\,\mathrm{d}\boldsymbol{r} \approx \hbar\omega\int |\alpha_{\boldsymbol{k}}|^2\,\mathrm{d}\boldsymbol{k}, \tag{48}$$

where we used $(\hat{E}^T)^+|\boldsymbol{\alpha}\rangle = 2^{-1}\boldsymbol{E}_\omega^T \mathrm{e}^{-\mathrm{i}\omega t}|\boldsymbol{\alpha}\rangle$ for coherent states and an equivalent relation for the $\hat{B}$ field operator. If we now insert instead the coherent state given by the amplitude $\partial_\theta\boldsymbol{\alpha}$ into the relation then we get

$$\frac{1}{4}\int \epsilon_0|\partial_\theta\boldsymbol{E}_\omega^T|^2 + \mu_0^{-1}|\partial_\theta\boldsymbol{B}_\omega|^2\,\mathrm{d}\boldsymbol{r} \approx \hbar\omega\int |\partial_\theta\alpha_{\boldsymbol{k}}|^2\,\mathrm{d}\boldsymbol{k}. \tag{49}$$

To see this, we note that the quantization of the electromagnetic field does not depend on θ and thus the corresponding field solutions $\boldsymbol{E}_{\boldsymbol{k}}$ with $(\hat{E}^T)^+ = \int \boldsymbol{E}_{\boldsymbol{k}}\hat{a}_{\boldsymbol{k}}\,\mathrm{d}\boldsymbol{k}$ also do not depend on θ. This implies that the θ dependence is only contained inside the complex amplitude $\boldsymbol{\alpha}$.

Finally, we can connect the QFI for coherent states, given by $\mathcal{I} = 4\int |\partial_\theta\alpha_{\boldsymbol{k}}|^2\,\mathrm{d}\boldsymbol{k}$ and by using eq. (49), to the integrated FI density

$$\mathcal{I}(\theta) = \frac{1}{\hbar\omega}\int \epsilon_0|\partial_\theta\boldsymbol{E}_\omega^T|^2 + \mu_0^{-1}|\partial_\theta\boldsymbol{B}_\omega|^2\,\mathrm{d}\boldsymbol{r}. \tag{50}$$

This shows that the integrated FI density yields the QFI at each point in time, justifying the definition of the FI density.

S.7.2 QFI in the Presence of Matter

The situation gets more complicated in a system with matter that interacts with the electromagnetic field. While the QFI constitutes the maximum FI that any measurement device can measure on a given state, in reality all measurement devices are also part of the physical world and thus perturb the system. While in the far field this can be neglected, in areas where the measurement device couples to the FI sources (i.e., in close proximity to the FI sources), we can expect a deviation from our theory. A recent study [9] has even suggested that this can be used to amplify the QFI for detectors in close proximity of the target.

This discussion shows some similarities to the Abraham-Minkowski debate [10, 11] about how the momentum inside a macroscopic medium can be separated into parts associated with the field and the matter. One of the central insights in this debate has been that, depending on the experimental setup, different definitions of the field momentum have to be used. In our case, depending on the working principle of the detector, different subsystems of the full quantum state are measured (due to differences in the matter-detector coupling), resulting in differences in the QFI.

On the other hand, if we neglect this coupling and assume that the quanta of the free field Hamiltonian get measured, then we can again connect the FI density and the QFI. To see this connection, we take the Hamiltonian describing the full matter-field system [12]

$$\hat{H} = \hat{H}_{\mathrm{em}} + \hat{H}_{\mathrm{mat}} + \hat{H}_{\mathrm{int}} \,. \tag{51}$$

Here $\hat{H}_{\mathrm{em}}$ corresponds to the Hamiltonian of the free field, the contribution of the dressed matter part is given by the dressed matter operator $\hat{B}(\boldsymbol{k}, \nu)$ (not to be confused with the magnetic field operator) such that

$$\hat{H}_{\mathrm{mat}} = \int \int_0^\infty \hbar \nu \hat{B}^\dagger(\boldsymbol{k}, \nu) \hat{B}(\boldsymbol{k}, \nu) \, \mathrm{d}\nu \, \mathrm{d}\boldsymbol{k} \,, \tag{52}$$

and the interaction takes on the following form

$$\hat{H}_{\mathrm{int}} = \int \int_0^\infty \hbar \xi(\boldsymbol{k}, \nu) \hat{B}^\dagger(\boldsymbol{k}, \nu) (\hat{a}_{\boldsymbol{k}} + \hat{a}^\dagger_{-\boldsymbol{k}}) \, \mathrm{d}\nu \, \mathrm{d}\boldsymbol{k} + \mathrm{H.c.} \,. \tag{53}$$

Here, $\xi(\boldsymbol{k}, \nu)$ describes the strength of interaction between the free field and the dressed matter [12]. We now apply the rotating wave approximation on the interaction term

$$\hat{H}^{\mathrm{RWA}}_{\mathrm{int}} = \int \int_0^\infty \hbar \xi(\boldsymbol{k}, \nu) \hat{B}^\dagger(\boldsymbol{k}, \nu) \hat{a}_{\boldsymbol{k}} \, \mathrm{d}\nu \, \mathrm{d}\boldsymbol{k} + \mathrm{H.c.} \,, \tag{54}$$

to guarantee that a system starting in a coherent state stays coherent. This directly allows us to transfer the proof from the free fields (see Sec. S.7.1) to the light-matter system. Overall, this shows that the FI density in the transversal part of the fields $u_{EM,T} = \frac{1}{\hbar\omega}\epsilon_0|\partial_\theta \boldsymbol{E}_\omega^T|^2 + \mu_0^{-1}|\partial_\theta \boldsymbol{B}_\omega|^2$ determines the QFI content of the photons. If we now add the components stored inside the polarization and magnetization of the matter (see Sec. S.2.1) and in the longitudinal components of the electric field, then we arrive at the FI density given in the main text.

References

[1] Hecht, E.: Optik. De Gruyter, Berlin, Boston (2018). https://doi.org/10.1515/9783110526653

[2] Hüpfl, J., Bachelard, N., Kaczvinszki, M., Horodynski, M., Kühmayer, M., Rotter, S.: Optimal cooling of multiple levitated particles: Theory of far-field wavefront shaping. Phys. Rev. A **107**(2) (2023)

[3] Bouchet, D., Rotter, S., Mosk, A.P.: Maximum information states for coherent scattering measurements. Nature Physics **17**(5), 564–568 (2021). https://doi.org/10.1038/s41567-020-01137-4

[4] Visser, H.J.: Antenna Theory and Applications. John Wiley & Sons, Hoboken, New Jersey (2012). https://doi.org/10.1002/9781119944751.fmatter

[5] Schöberl, J., et al.: Finite element package Netgen/NGSolve. NGSolve (2023)

[6] Mandel, L., Wolf, E.: Optical Coherence and Quantum Optics. Cambridge university press, Cambridge (1995). https://doi.org/10.1017/CBO9781139644105

[7] Le Cam, L.: An approximation theorem for the Poisson binomial distribution. (1960)

[8] Keller, O.: Quantum Theory of Near-field Electrodynamics. Springer, Berlin Heidelberg (2012). https://doi.org/10.1007/978-3-642-17410-0

[9] Kienesberger, L., Juffmann, T., Nimmrichter, S.: Quantum Limits of Position and Polarizability Estimation in the Optical Near Field (2023). https://doi.org/10.48550/arXiv.2307.02348

[10] Barnett, S.M.: Resolution of the Abraham-Minkowski dilemma. Physical Review Letters **104**, 070401 (2010). https://doi.org/10.1103/PhysRevLett.104.070401

[11] Kinsler, P., Favaro, A., McCall, M.W.: Four Poynting theorems. European Journal of Physics **30**(5), 983 (2009). https://doi.org/10.1088/0143-0807/30/5/007

[12] Huttner, B., Barnett, S.M.: Quantization of the electromagnetic field in dielectrics. Phys. Rev. A **46**, 4306–4322 (1992). https://doi.org/10.1103/PhysRevA.46.4306